



1 **Sea Ice Changes in the Southwest Pacific Sector of the Southern Ocean During**
2 **the Last 140,000 Years**

3
4 Jacob Jones¹, Karen E Kohfeld^{1,2}, Helen Bostock^{3,4}, Xavier Crosta⁵, Melanie Liston⁶, Gavin Dunbar⁶, Zanna Chase⁷, Amy Leventer⁸
5 Harris Anderson⁷, Geraldine Jacobsen⁹

6
7 ¹ School of Resource and Environmental Management, Simon Fraser University, Burnaby, Canada

8 ² School of Environmental Science, Simon Fraser University, Burnaby, Canada

9 ³ School of Earth and Environmental Sciences, The University of Queensland, Brisbane, Australia

10 ⁴ National Institute of Water and Atmospheric Research (NIWA), Wellington, New Zealand

11 ⁵ Université de Bordeaux, CNRS, EPHE, UMR 5805 EPOC, Pessac, France

12 ⁶ Antarctic Research Centre, Victoria University of Wellington, Wellington, New Zealand

13 ⁷ Institute of Marine and Antarctic Studies, University of Tasmania, Hobart, Australia

14 ⁸ Geology Department, Colgate University, Hamilton, NY, USA

15 ⁹ Australian Nuclear Science and Technology (ANSTO), Lucas Heights, New South Wales, Australia

16
17 *Correspondence to:* Jacob Jones (jacob_jones@sfu.ca)

18 **Abstract**

19 Sea ice expansion in the Southern Ocean is believed to have contributed to glacial-interglacial
20 atmospheric CO₂ variability by inhibiting air-sea gas exchange and influencing the ocean's
21 meridional overturning circulation. However, limited data on past sea ice coverage over the last
22 140 ka (a complete glacial cycle) have hindered our ability to link sea ice expansion to oceanic
23 processes that affect atmospheric CO₂ concentration. Assessments of past sea ice coverage
24 using diatom assemblages have primarily focused on the Last Glacial Maximum (~21 ka) to
25 Holocene, with few quantitative reconstructions extending to the onset of glacial Termination II
26 (~135 ka). Here we provide new estimates of winter sea ice concentrations (wSIC) and summer
27 sea surface temperatures (sSSTs) for a full glacial-interglacial cycle from the southwestern
28 Pacific sector of the Southern Ocean using fossil diatom assemblages from deep-sea core
29 TAN1302-96 (59.09°S, 157.05°E, water depth 3099 m). We find that winter sea ice was
30 consolidated over the core site during the latter part of the penultimate glaciation, Marine
31 Isotope Stage (MIS) 6 (from at least 140 to 134 ka), when sSSTs were between ~1 and 1.5°C.
32 The winter sea ice edge then retreated rapidly as sSSTs increased during the transition into the
33 Last Interglacial Period (MIS 5e), reaching ~4.5°C by 125 ka. As the Earth entered the early
34 glacial stages, sSSTs began to decline around 112 ka, but winter sea ice largely remained absent
35 until ~65 ka during MIS 4, when it was sporadically present but unconsolidated (<40% wSIC).
36 WSIC and sSSTs reached their maximum concentration and coolest values by 24.5 ka, just prior
37 to the Last Glacial Maximum. Winter sea ice remained absent throughout the Holocene, while
38 sSSTs briefly exceeded modern values, reaching ~5°C by 11.4 ka, before decreasing to ~4°C and
39 stabilizing. The absence of sea ice coverage over the core site during the early glacial period
40 suggests that sea ice may not have been a major contributor to CO₂ drawdown at this time.
41 During MIS 5d, we observe a weakening of meridional SST gradients between 42° to 59°S
42 throughout the region, which may have contributed to early reductions in atmospheric CO₂
43 concentrations through its impact on air-sea gas exchange. Sea ice expansion during MIS 4,
44 however, coincides with observed reductions in Antarctic Intermediate Water production and



45 subduction, suggesting that sea ice may have influenced intermediate ocean circulation
46 changes.

47

48 **1.0 Introduction**

49 Antarctic sea ice has been suggested to have played a key role in glacial-interglacial
50 atmospheric CO₂ variability (e.g., Stephens & Keeling, 2000; Ferrari et al., 2014; Kohfeld &
51 Chase, 2017; Stein et al., 2020). Sea ice has been dynamically linked to several processes that
52 promote deep ocean carbon sequestration, namely by: [1] reducing deep ocean outgassing by
53 ice-induced ‘capping’ and surface water stratification (Stephens & Keeling, 2000; Rutgers van
54 der Loeff et al., 2014), and [2] influencing ocean circulation through water mass formation and
55 deep-sea stratification, leading to reduced diapycnal mixing and reduced CO₂ exchange
56 between the surface and deep ocean (Toggweiler, 1999; Bouttes et al., 2010; Ferrari et al.,
57 2014). Numerical modelling studies have shown that sea ice-induced capping, stratification, and
58 reduced vertical mixing may be able to account for a significant portion of the total CO₂
59 variability on glacial-interglacial timescales (between 40-80 ppm) (Stephens & Keeling, 2000;
60 Galbraith & de Lavergne, 2018; Marzocchi & Jansen, 2019; Stein et al., 2020). However, debate
61 continues surrounding the timing and magnitude of sea ice impacts on glacial-scale carbon
62 sequestration (e.g., Morales Maqueda & Rahmstorf, 2002; Archer et al., 2003; Sun &
63 Matsumoto, 2010; Kohfeld & Chase, 2017).

64 Past Antarctic sea ice coverage has been estimated primarily through diatom-based
65 reconstructions, with most work focusing on the Last Glacial Maximum (LGM), specifically the
66 EPILOG timeslice as outlined in Mix et al. (2001), corresponding to 23 to 19 thousand years ago
67 (ka). During the LGM, these reconstructions suggest that winter sea ice expanded by 7-10°
68 latitude (depending on the sector of the Southern Ocean), which corresponds to an
69 approximate doubling of total winter sea ice coverage compared to modern observations
70 (Gersonde et al., 2005; Benz et al., 2016). Currently, only a handful of studies provide
71 quantitative sea ice coverage estimates back to the penultimate glaciation, Marine Isotope
72 Stage (MIS) 6 (~194 to 135 ka) (Gersonde & Zielinski, 2000; Crosta et al., 2004; Schneider-Mor
73 et al., 2012; Esper & Gersonde 2014; Ghadi et al. 2020). These studies primarily cover the
74 Atlantic sector, with only one published sea ice record from each of the Indian (SK200-33 from



75 Ghadi et al., 2020), eastern Pacific (PS58/271-1 from Esper & Gersonde, 2014), and
76 southwestern Pacific sectors (SO136-111 from Crosta et al., 2004). These glacial-interglacial sea
77 ice records show heterogeneity between sectors in both timing and coverage. While the
78 Antarctic Zone (AZ) in the Atlantic sector experienced early sea ice advance corresponding to
79 MIS 5d cooling (i.e., 115 to 105 ka) (Gersonde & Zielinski, 2000; Bianchi & Gersonde, 2002;
80 Esper & Gersonde, 2014), the Indian and Pacific sector cores in the AZ show only minor sea ice
81 advances during this time (Crosta et al., 2004; Ghadi et al., 2020). The lack of spatial and
82 temporal resolution has resulted in significant uncertainty in our ability to evaluate the timing
83 and magnitude of sea ice change during a full glacial cycle across the Southern Ocean, and to
84 link sea ice to glacial-interglacial CO₂ variability.

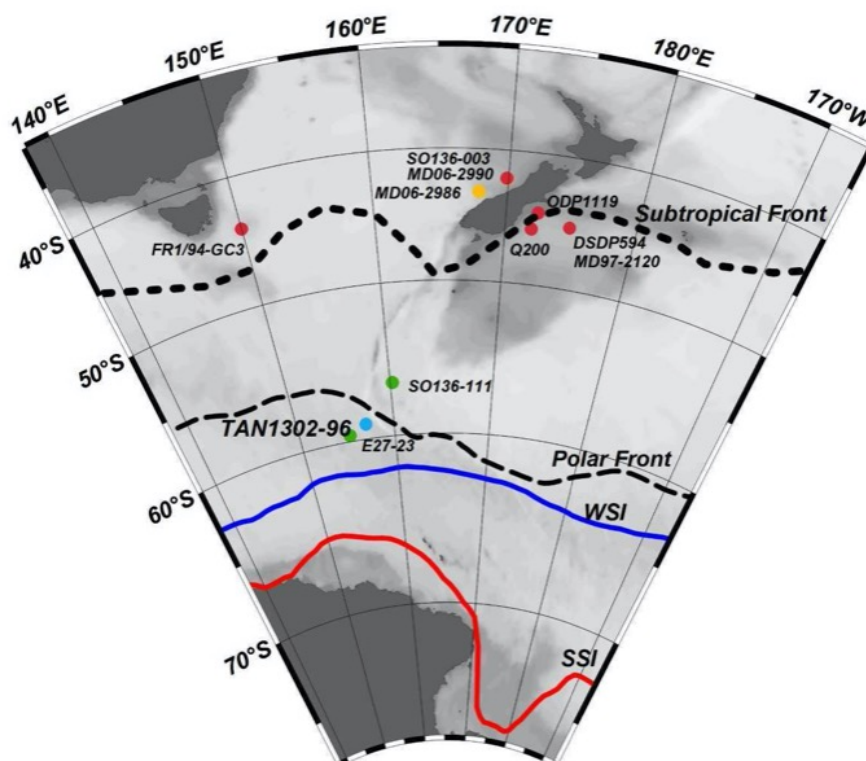
85 This paper provides new winter sea ice concentration (wSIC) and summer sea surface
86 temperature (sSST) estimates for the southwestern Pacific sector of the Southern Ocean over
87 the last 140 ka. SSSTs and wSIC are estimated by applying the Modern Analog Technique (MAT)
88 to fossil diatom assemblages from sediment core TAN1302-96 (59.09°S, 157.05°E, water depth
89 3099 m). We place this record within the context of sea ice and sSST changes from the region
90 using previously published records from SO136-111 (56.66°S, 160.23°E, water depth 3912 m),
91 which has recalculated wSIC and sSST estimates presented in this study, and nearby marine
92 core E27-23 (59.61°S, 155.23°E; water depth 3182 m) (Ferry et al., 2015). Using these records,
93 we compare the timing of sea ice expansion to early glacial-interglacial CO₂ variability to test
94 the hypothesis that the initial CO₂ drawdown (~115 to 100 ka) resulted from reduced air-sea
95 gas exchange in response to sea ice capping and surface water stratification. We then consider
96 alternative oceanic drivers of early atmospheric CO₂ variability, and place our sSSTs estimates
97 within the context of other studies to examine how regional cooling and a weakening in
98 meridional SST gradients might affect air-sea disequilibrium and early CO₂ drawdown (Khatiwala
99 et al., 2019). Finally, we compare our wSIC estimates with regional reconstructions of Antarctic
100 Intermediate Water (AAIW) production and subduction variability using previously published
101 carbon isotope analyses on benthic foraminifera from intermediate to deep-water depths in the
102 southwest Pacific sector of the Southern Ocean to test the hypothesis that sea ice expansion is
103 dynamically linked to AAIW production and variability (Ronge et al., 2015).



104 2.0 Methods

105 2.1 Study Site & Age Determination

106 We reconstruct diatom-based wSIC and sSST using marine sediment core TAN1302-96
107 (59.09°S, 157.05°E, water depth 3099 m) (Figure 1). The 364 cm core was collected in March
108 2013 using a gravity corer during the return of the *RV Tangaroa* from the Mertz Polynya in
109 Eastern Antarctica (Williams et al., 2013). The core is situated in the western Pacific sector of
110 the Southern Ocean, on the southwestern side of the Macquarie Ridge, approximately 3-4°
111 south of the average position of the Polar Front (PF) at 157°E (Sokolov & Rintoul, 2009).



112
113 **Figure 1:** Map of the southwestern Pacific sector of the Southern Ocean including the study
114 site, TAN1302-96 (blue circle), and additional cores providing supporting information on sea ice
115 extent, SO136-111 and E27-23 (green circles), SST reconstructions (red circles), and $\delta^{13}\text{C}$ of
116 benthic foraminifera (yellow circles). Metadata for these cores are provided in Table A1.
117 Dashed lines show the average location of the Subtropical and Polar Fronts (Smith et al., 2013;



118 Bostock et al., 2015), red and blue lines show approximate positions of summer and winter sea
119 ice extents, respectively (Reynolds et al., 2002; 2007).

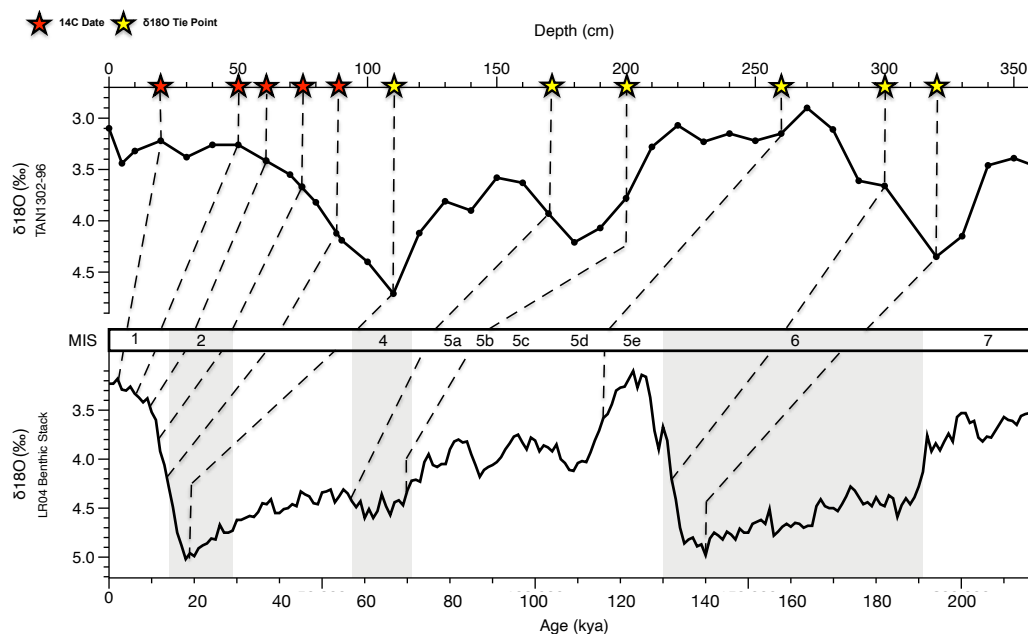
120

121 The age model for TAN1302-96 (Figures 2 and 3) was based on a combination of
122 radiocarbon dating of mixed foraminiferal assemblages, and stable oxygen isotope stratigraphy
123 on *Neogloboquadrina pachyderma* (180-250 μm). Seven accelerator mass spectrometry (AMS)
124 ^{14}C samples were collected (Table A1 in Appendix A) and consisted of mixed assemblages of
125 planktonic foraminifera (*N. pachyderma* and *Globigerina bulloides*, $>250 \mu\text{m}$). Three of the
126 seven radiocarbon samples (NZA 57105, 57109, and 61429) were previously published in
127 Prebble et al., (2017), and four additional samples (OZX 517-520) were added to improve the
128 dating reliability (Table A1 in Appendix A). OZX 519 and OZX 520 produced dates that were not
129 distinguishable from background ($>57.5 \text{ ka}$) and were subsequently excluded from the age
130 model. The TAN1302-96 oxygen isotopes were run at the National Institute of Water and
131 Atmospheric Research (NIWA) using the Kiel IV individual acid-on-sample device and analysed
132 using Finnigan MAT 252 Mass Spectrometer. The precision is $\pm 0.07\%$ for $\delta^{18}\text{O}$ and $\pm 0.05\%$ for
133 $\delta^{13}\text{C}$.

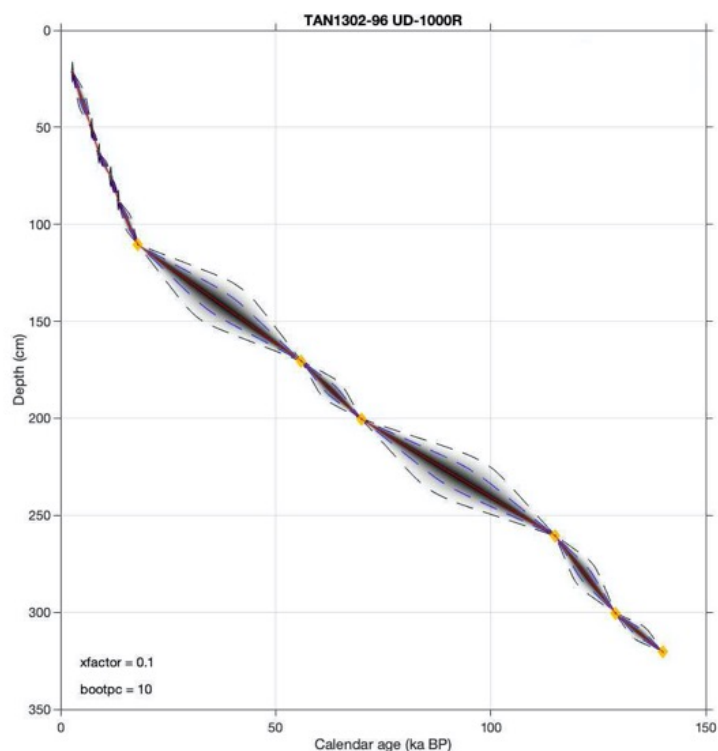
134 The age model was constructed using the 'Undatable' MATLAB software by
135 bootstrapping at 10% and using an x-factor of 0.1 (Lougheed & Obrochta, 2019), which scales
136 Gaussian distributions of sediment accumulation uncertainty (Table A2 in Appendix A). Below
137 100 cm, six tie points were selected at positions of maximum change in $\delta^{18}\text{O}$ and were
138 correlated to the LR04 benthic stack (Lisiecki & Raymo, 2005) (Fig 2; Table A2 in Appendix A).
139 We used a conservative marine reservoir age (MRA) for radiocarbon calibration of 1000 ± 50
140 years, in line with regional estimates in Paterne et al. (2019) and modelled estimates by Butzin
141 et al. (2017; 2020). The age model shows that TAN1302-96 extends to at least 140 ka, capturing
142 a full glacial-interglacial cycle. Linear sedimentation rates (LSR) in TAN 1302-96 were observed
143 to be higher during interglacial periods, averaging 3.37cm/ka , compared to glacial periods,
144 averaging 2.74cm/ka . It is worth noting that there can be significant MRA variability over time
145 due changes in ocean ventilation, sea ice coverage, and wind strength, specifically in the polar



146 high latitudes (Heaton et al., 2020), and as a result, caution should be taken when interpreting
147 the precision of radiocarbon dates.



148 **Figure 2:** Age model of TAN1302-96. Red stars indicate the depth of AMS ^{14}C samples, and
149 yellow stars indicate tie points between the TAN1302-96 oxygen isotope stratigraphy and the
150 LR04 benthic stack (Lisiecki & Raymo, 2005). Two radiocarbon dates, OZX 519 & 520, were not
151 included in the age model as they produced dates that were NDFB (not distinguishable from
152 background).



153 **Figure 3:** Age model of TAN1302-96. Tie points are depicted as yellow dots and grey shading
154 represents associated uncertainty between tie points. The age model used a marine reservoir
155 calibration of 1000 +/- 50 years.
156

157 2.2 Diatom Analysis

158 TAN1302-96 was sampled every 3-4 cm throughout the core except between 130-180
159 cm, where samples were collected every 10 cm due to limited availability of sample materials
160 (Table A3 in Appendix A). Diatom slide preparation followed two procedures. The first approach
161 approximated the methods outlined in Renberg (1990), while the second followed the protocol
162 outlined in Warnock & Scherer (2014). To ensure there were no biases between preparation
163 techniques, results from each technique were first visually compared followed by a comparison
164 of sample means (see Figure B1 in Appendix B). No biases in the data were observed between
165 methods.



166 The first procedure was conducted at Victoria University of Wellington and Simon Fraser
167 University on samples every 10 cm throughout the core. Sediment samples contained high
168 concentrations of diatoms with little carbonaceous or terrigenous materials, so no dissolving
169 aids were used. Instead, approximately 50 mg of sediment was weighed, placed into a 50 ml
170 centrifuge tube, and topped up with 40 ml of deionized water. Samples were then manually
171 shaken to disaggregate sediment, followed by a 10-second mechanical stir using a vortex
172 machine. Samples were then left to settle for 25 seconds. 0.25 mL of the solution was then
173 pipetted onto a microscope slide from a consistent depth, where it was left to dry overnight.
174 Once the sample had dried, coverslips were permanently mounted to the slide using Permout,
175 a high refractive index mountant. Slides were redone if they contained too many diatoms and
176 identification was not possible, or if they contained too few diatoms (generally <40 specimens
177 per transect). Sediment sample weight was adjusted to achieve the desired dilution.

178 The second procedure was conducted at Colgate University on samples every 3-4 cm
179 throughout the core. Oven-dried samples were placed into a 20 ml vial with 1-2 ml of 10% H₂O₂
180 and left to react for up to several days, followed by a brief (2-3 second) ultrasonic bath to
181 disaggregate samples. The diatom solution was then added into a settling chamber, where
182 microscope coverslips were placed on stages to collect settling diatoms. The chamber was
183 gradually emptied through an attached spigot, and samples were evaporated overnight. Cover
184 slips were permanently mounted onto the slides with Norland Optical Adhesive #61, a
185 mounting medium with a high refractive index.

186 Diatom identification was conducted at Simon Fraser University using a Leica Leitz
187 DMBRE light microscope using standard microscopy techniques. Following transverses, a
188 minimum of 300 individual diatoms were identified at 1000x magnification from each sample
189 throughout the core. Individuals were counted towards the total only if they represented at
190 least one-half of the specimen so that fragmented diatoms were not counted twice.
191 Identification was conducted to the highest taxonomic level possible, either to the species or
192 species-group level. Taxonomic identification was conducted using numerous identification
193 materials, including (but not limited to): Fenner et al. (1976); Fryxell & Hasle (1976; 1980);
194 Johansen & Fryxell (1985); Hasle & Syversten (1997); Cefarelli et al. (2010); and Wilks & Armand



195 (2017). Diatom species that have similar environmental preferences were grouped together as
196 outlined in Crosta et al. (2004). Three main taxonomic groups were established, and their
197 relative abundances were calculated by dividing the number of identified specimens of a
198 particular species by the total number of identified diatoms from the sample. The following
199 main taxonomic groups were used (Table 1):

200

201 [1] Sea Ice Group: representing diatoms that thrive in or near the sea ice margin in SSTs
202 generally ranging from -1 to 1 °C.

203 [2] Permanent Open Ocean Zone (POOZ): representing diatoms that thrive in open
204 ocean conditions, with SSTs generally ranging from ~2 to 10 °C.

205 [3] Sub-Antarctic Zone (SAZ): representing diatoms that thrive in warmer sub-Antarctic
206 waters, with SSTs generally ranging from 11 to 14 °C.

207

208 **Table 1:** Species comprising each of the diatom taxonomic groups (updated from Crosta et al.,
209 2004).

Sea Ice Group	POOZ Group	SAZ Group
<i>Actinocyclus actinochilus</i>	<i>Fragilariopsis kerguelensis</i>	<i>Azpeitia tabularis</i>
<i>Fragilariopsis curta</i>	<i>Fragilariopsis rhombica</i>	<i>Hemidiscus cuneiformis</i>
<i>Fragilariopsis cylindrus</i>	<i>Fragilariopsis separanda</i>	<i>Thalassionema nitzschioides</i> var. <i>lanceolata</i>
<i>Fragilariopsis obliquecostata</i>	<i>Rhizosolenia polydactyla</i> var. <i>polydactyla</i>	<i>Thalassiosira eccentrica</i>
<i>Fragilariopsis ritscheri</i>	<i>Thalassionema nitzschioides</i> (form 1)	<i>Thalassiosira oestrupii</i> gp.
<i>Fragilariopsis sublinearis</i>	<i>Thalassiosira gracilis</i> gp.	
	<i>Thalassiosira lentiginosa</i>	
	<i>Thalassiosira oliverana</i>	
	<i>Thalassiothrix</i> sp.	
	<i>Trichotoxon reinboldii</i>	

210

211 2.3 Modern Analog Technique

212 Past wSIC and sSSTs (January to March) were estimated for TAN1302-96 and
213 recalculated for SO136-111 by applying the Modern Analog Technique (MAT) to the fossil
214 diatom assemblages, as outlined in Crosta et al. (1998; 2020). The MAT reference database
215 used for this analysis is comprised of 249 modern core top samples (analogs) located primarily
216 in the Atlantic and Indian sectors from ~40°S to the Antarctic coast. The age of the core tops



217 included in the reference database have been assessed through radiocarbon and/or isotope
218 stratigraphy when possible. Core tops were visually evaluated for selective diatom dissolution,
219 so it is believed that sub-modern assemblages contain well-preserved and unbiased specimens.
220 Modern summer SSTs and wSIC were interpolated from the reference core locations using a
221 $1^{\circ} \times 1^{\circ}$ grid from the World Ocean Atlas (Locarnini et al., 2013) through the Ocean Data View
222 (Schlitzer, 2005). The MAT was applied using the “bioindic” package (Guiot & de Vernal, 2011)
223 through the R-platform. Fossil diatom assemblages were compared to the modern analogs
224 using 33 species or species-groups to identify the five most similar modern analogs using both
225 the LOG and CHORD distance. The reconstructed sSST and wSIC are the distance-weighted
226 mean of the climate values associated with the selected modern analog (Guiot et al., 1993;
227 Ghadi et al., 2020). Both MAT approaches produce an R^2 value of 0.96 and a root mean square
228 error of prediction (RMSEP) of $\sim 1^{\circ}\text{C}$ for summer SST, and an R^2 of 0.93 and a RMSEP of 10% for
229 wSIC (Ghadi et al. 2020). As outlined in Ferry et al., (2015), we consider $<15\%$ wSIC to represent
230 an absence of winter sea ice, 15-40% wSIC as present but unconsolidated, and $>40\%$ to
231 represent consolidated winter sea ice.

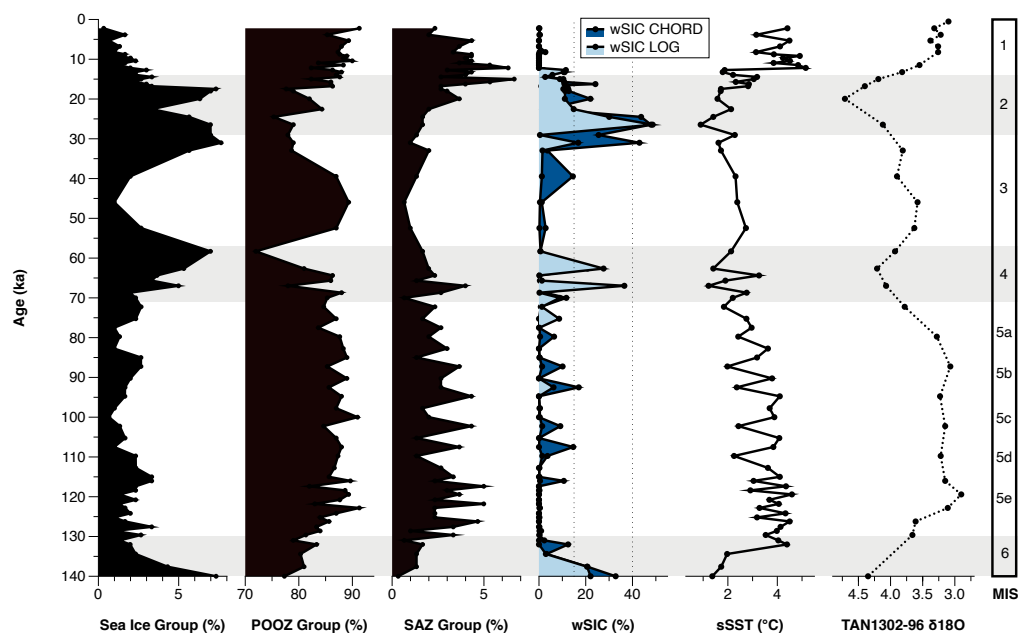


232

233 3.0 Results

234 3.1 Diatom Assemblage Results

235 Fifty-one different species or species groups were identified, of which 33 were used in
236 the transfer function. Polar Open Ocean Zone (POOZ) diatoms made up the largest proportion
237 of diatoms identified, representing between 72-91% of the assemblage (Figure 4), with higher
238 values observed during warmer interstadial periods of MIS 1, 3, and 5. Sea ice diatoms made up
239 the second most abundant group, representing between 0.5-7.5% of the assemblage, with
240 higher values observed during cooler stadial periods (MIS 2, 4, and 6). The Sub-Antarctic Zone
241 group had relatively low abundances, with higher SAZ values occurring during warmer
242 interstadial periods.



243

244 **Figure 4:** Diatom assemblages results from TAN1302-96 separated into % contribution from
245 each taxonomic group (Sea ice Group, POOZ, & SAZ; see Table 1) over a full glacial-interglacial
246 cycle. Using the Modern Analog Technique (MAT), winter sea ice concentration (wSIC) and
247 summer sea surface temperature (sSST) were estimated and compared against the $\delta^{18}\text{O}$
248 signature of TAN1302-96.

249



250

251 **3.2 TAN1302-96 Summer SST and wSIC Estimates**

252 Estimates of sSST and wSIC from both LOG and CHORD MAT outputs produced similar
253 results (Figure 4). During Termination II, sSSTs began to rise from ~1°C at 140 ka (MIS 6) to 4.5°C
254 at 130 ka (MIS 5e/6 boundary). This warming corresponded with a decrease in wSIC from 48%
255 to approximately 0% over the same time periods (Figure 4). Reconstructed sSSTs continued to
256 rise slightly throughout MIS 5e, reaching a maximum value of 4.6°C at 118 ka, after which they
257 declined throughout MIS 5. During this period of sSST decline, winter sea ice was largely absent,
258 punctuated by brief periods during which sea ice was present but unconsolidated (wSIC of
259 14.7% and 17% at 105 and 90 ka, respectively). During MIS 4 (71 to 57 ka), sSSTs cooled to
260 between roughly 1°C and 3°C, and sea ice expanded to 36%, such that it was present but
261 unconsolidated for intervals of a few thousand years. sSSTs increased slightly from 1.5°C at 61
262 ka (during MIS 4) to ~2.5°C at 50 ka (during MIS 3), followed by a general cooling trend into MIS
263 2. Sea ice appears to have been largely absent during MIS 3 (57 to 29 ka), although sampling
264 resolution is low, but increased rapidly to 48% cover during MIS 2 where winter sea ice was
265 consolidated over the core site. During MIS 2, sSSTs cooled to a minimum of <1°C at 24.5 ka.
266 After 18 ka, the site rapidly transitioned from cool, ice-covered conditions to warmer, ice-free
267 winter conditions during the early deglaciation. This warming was interrupted by a brief cooling
268 around 13.5 ka, following which sSSTs quickly reached their maximum values of ~5°C at 11.4 ka
269 and remained relatively high throughout the rest of the Holocene. Winter sea ice was not
270 present during the Holocene. There were no non-analog conditions observed in TAN1302-96
271 samples.

272

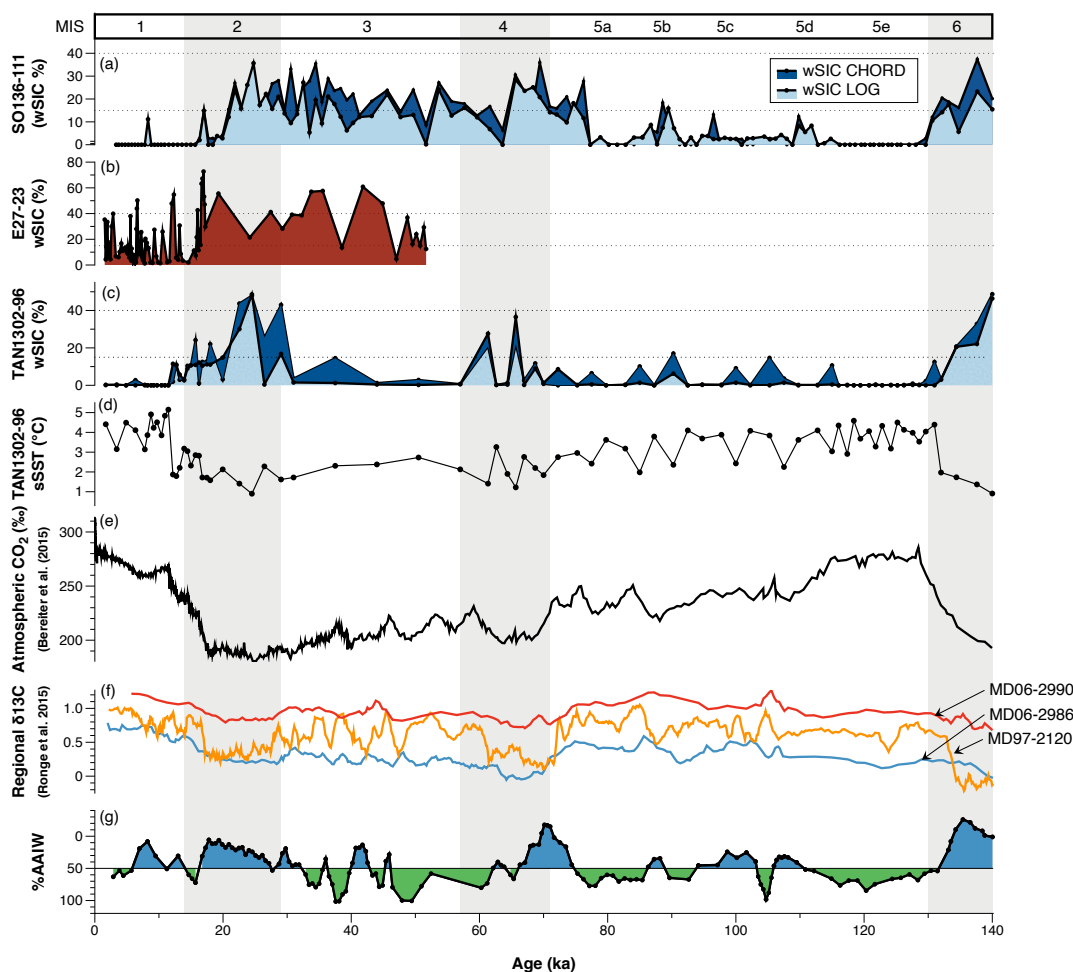
273 **4.0 Discussion**

274 **4.1 Regional sSST and wSIC Estimates**

275 The new wSIC and sSST estimates from TAN1302-96 and recalculated wSIC estimates
276 from SO136-111 show a coherent regional pattern (Figure 5). Both cores show relatively high
277 concentrations of sea ice during MIS 2, 4, and 6, with lower values during MIS 1 and 5.
278 TAN1302-96 shows slightly higher concentrations during MIS 2 (47%) and 4 (37%) compared
279 with SO136-111 (35% and 36%, respectively), which can be explained by a more poleward



280 position of TAN1302-96 relative to SO136-111. The estimates between cores differ during MIS
281 3, with seemingly lower wSIC in TAN1302-96 than in SO136-111, which might result from the
282 low sampling resolution in TAN1302-96 during this period. Overall, these cores show a highly
283 similar and coherent history of sea ice over the last 140 ka.



284
285 **Figure 5:** (a) wSIC estimates using MAT from SO136-111 (recalculated in this study, see
286 Appendix D); (b) wSIC estimates using GAM from E27-23 (Ferry et al., 2015); (c) wSIC estimates
287 using MAT from TAN1302-96 (this study); (d) sSST estimates using MAT from TAN1302-96 (this
288 study); (e) Antarctic atmospheric CO₂ concentrations over 140 ka (Bereiter et al., 2015); (f) $\delta^{13}\text{C}$
289 data from nearby cores MD06-2990/SO136-003, MD97-2120, and MD06-2986 (Ronge et al.,
290 2015); (g) %Antarctic Intermediate Water (%AAIW) as calculated in Ronge et al. (2015), which



291 tracks when core MD97-2120 was bathed primarily by AAIW (green) or Upper Circumpolar
292 Deep Water (UCDW) (blue).
293

294 When compared with E27-23 (Figure 5), which is located only ~120 km to the southwest
295 of TAN1302-96 (Figure 1), the TAN1302-96 core shows lower estimates of wSIC, especially
296 during MIS 3. During early and mid-MIS 2, both cores show similar wSIC estimates, while later in
297 MIS 2 (~17 ka), E27-23 reports a maximum wSIC of 72% compared to only 22% at TAN1302-96.
298 A discrepancy between estimates is also observed during the Holocene, with E27-23 reporting
299 sea ice estimates of up to nearly 50% during the mid-Holocene (~6 ka), while TAN1302-96
300 experienced values well below the RMSEP of 10%.

301 Possible explanations for the observed differences in wSIC estimates include: [1]
302 differences in laboratory protocols; [2] differences in diatom identification/counting
303 methodology; [3] differences in statistical applications; [4] selective diatom dissolution; and [5]
304 differences in the redistribution of sediment by the Antarctic Circumpolar Current (ACC)
305 between each of the core sites. Of these explanations, we believe that [3] and [5] are the most
306 likely candidates and are discussed below (for further discussion on [1], [2], and [4], see
307 Appendix C).

308 The first possible explanation we identified is through the use of different statistical
309 applications. Ferry et al. (2015) used a Generalized Additive Model (GAM) to estimate wSIC for
310 both E27-23 and SO136-111, while we have used the MAT for TAN1302-96 and SO136-111. A
311 simple comparison of wSIC estimates between the results in Ferry et al. (2015) and our
312 recalculated wSIC estimates for SO136-111 can provide insights into the magnitude of
313 estimation differences. Generally speaking, the GAM estimation produced higher wSIC
314 estimates than the MAT (e.g., ~50% wSIC at 23 ka while the MAT produced ~37% for the same
315 time period); however, we believe it is unlikely that statistical approaches alone could explain a
316 larger difference (i.e., 50%) between E27-23 and TAN1302-96.

317 The second possible explanation is through lateral sediment redistribution and focusing
318 by the ACC. We estimated sediment focusing for E27-23 using ^{230}Th data from Bradtmiller et al.
319 (2009) together with dry bulk density estimated using calcium carbonate content (Froelich,



320 1991). Both sedimentation rates and focusing factors for the E27-23 are relatively high (~35
321 cm/ka and max=26, respectively) during the LGM and Holocene, which could influence the
322 reliability of wSIC and sSST estimation (see Figure B2 in Appendix B). Several peaks in focusing
323 occurring around 16, 12, and 3 ka appear to closely correspond to periods of peak wSIC (~67%,
324 ~54%, and ~35%, respectively), suggesting a possible link. Lateral redistribution could artificially
325 increase or decrease relative abundances of some diatom groups, which could lead to over or
326 under estimations of sea ice coverage. Thorium analysis for TAN1302-96 is beyond the scope of
327 this study; however, future work could help address this uncertainty.

328 Although we are unable to identify the specific cause of the differences, we do suggest
329 using caution when interpreting the exact magnitude of sea ice expansion in this region, and to
330 consider the results from all cores when drawing conclusions of regional sea ice history.

331

332 **4.2 The Role of Sea Ice on Early CO₂ Drawdown**

333 Kohfeld & Chase (2017) hypothesized that the initial drawdown of atmospheric CO₂ (~35
334 ppm) during the glacial inception of MIS 5d (~115 to 100 ka) was primarily driven by sea ice
335 capping and a corresponding stratification of surface waters, which reduced the CO₂ outgassing
336 of upwelled carbon-rich waters. This hypothesis is supported by several lines of evidence,
337 including: [1] sea salt sodium (ssNA) archived in Antarctic ice cores, suggesting sea ice
338 expansion near the Antarctic continent (Wolf et al., 2010); [2] $\delta^{15}\text{N}$ proxy data from the central
339 Pacific sector of the Southern Ocean, suggesting increased stratification south of the modern-
340 day Antarctic Polar Front (Studer et al., 2015); and [3] diatom assemblages in the polar frontal
341 zone of the Atlantic sector, suggesting a slight cooling and northward expansion of sea ice
342 during MIS 5d (Bianchi & Gersonde, 2002). Our data address this hypothesis by providing
343 insights into early sea ice expansion into the polar frontal zone of the western Pacific sector.

344 Our data show that, in contrast to the Atlantic sector (Bianchi & Gersonde, 2002), there
345 was no sea ice advance into the modern-day PFZ of the SW Pacific during MIS5d. Neither
346 TAN1302-96 nor S0136-111 shows evidence of an early glacial increase in wSIC (Figure 5).
347 Unfortunately, the lack of spatially extensive quantitative records extending back to
348 Termination II limits our ability to estimate the timing and magnitude of sea ice changes for



349 regions poleward of 59°S in the southwestern Pacific. We anticipate, however, that an advance
350 in the sea ice edge, consistent with those outlined in Bianchi & Gersonde (2002), likely would
351 have reduced local SSTs as the sea ice edge advanced closer to the core site. Indeed, the
352 TAN1302-96 SST record does show a decrease to ~2°C (observed at 107 ka), which quickly
353 rebounded to ~4°C by ~105 ka (Figure 5). However, this sSST drop occurred roughly 8 ka after
354 the initial CO₂ reduction, suggesting that the CO₂ drawdown event and local sSST reduction may
355 not be linked. While the lack of sea ice diatoms and no discernable reductions of sSSTs occurred
356 during MIS 5d at TAN1302-96 or SO136-111, we cannot rule out the possibility that modest sea
357 ice advances, or a consolidation of pre-existing sea ice, took place south of the core sites.

358 Given that sea ice was not at its maximum extent during the early glacial, it stands to
359 reason that any reductions to air-sea gas exchange in response to the hypothetically expanded
360 sea ice would not have been at its maximum impact either. Thus, it is likely that any effects of
361 sea ice capping would not have reached their full potential during the early glacial period.
362 Previous modeling work has suggested that the maximum impact of sea ice expansion on
363 glacial-interglacial atmospheric CO₂ reductions ranged from 5 to 14 ppm (Kohfeld & Ridgwell,
364 2009). More recent modeling studies are consistent with this range, suggesting a 10-ppm
365 reduction (Stein et al., 2020), while some studies even suggest a possible increase in
366 atmospheric CO₂ concentrations due to sea ice expansion (Khatiwala et al., 2019). Furthermore,
367 Stein et al. (2020) suggest that the effects of sea ice capping would have taken place after
368 changes in deep ocean stratification had occurred and would have contributed to CO₂
369 drawdown later during the mid-glacial period. These model results, when combined with our
370 data, suggest that even if modest sea ice advances did take place during the early glacial (i.e.,
371 MIS 5d), their impacts on CO₂ variability would likely have been modest, ultimately casting
372 doubt on the hypothesis that early glacial CO₂ reductions of 35 ppm can be linked solely to the
373 capping and stratification effects of sea ice expansion.

374

375 **4.3 Other Potential Contributors to Early Glacial CO₂ Variability**

376 The changes observed in wSIC and sSST from TAN1302-96 suggests that sea ice
377 expansion was likely not extensive enough early in the glacial cycle for a sea ice capping effect



378 to be solely responsible for early atmospheric CO₂ drawdown. This leaves open the question of
379 what may have contributed to early drawdown of atmospheric CO₂. In terms of the ocean's
380 role, we highlight three contenders: [1] a potentially non-linear response between sea ice
381 coverage and CO₂ sequestration potential; [2] links between sea ice expansion and early
382 changes in global ocean overturning, and [3] the impact of cooling on air-sea disequilibrium in
383 the Southern Ocean.

384 The first possible explanation considers that not all sea ice has the same capacity to
385 facilitate or inhibit air-sea gas exchange. We previously suggested that because sea ice was not
386 at its maximum extent during MIS 5d, the contribution of sea ice on CO₂ sequestration would
387 likely not be at its maximum extent either. However, this assumes that there is a linear
388 relationship between sea ice coverage and CO₂ sequestration potential. We know that different
389 sea ice properties, such as thickness and temperature, determine overall porosity, with thicker
390 and colder sea ice being less porous and more effective at reducing air-sea gas exchange
391 compared to thinner and warmer sea ice (Delille et al., 2014). It is therefore possible that if
392 modest sea ice advances took place closer to the Antarctic continent (and were therefore not
393 captured by TAN1302-96), they may have been more effective at reducing CO₂ outgassing,
394 either by experiencing some type of reorganization or consolidation, or through a change in
395 properties such as temperature or thickness. It is also possible that sea ice coverage over some
396 regions leads to more effective capping, while in other regions sea ice growth contributes only
397 to marginal reductions in air-sea gas exchange. This, theoretically, could point to a non-linear
398 response between sea ice expansion and CO₂ sequestration potential, and could link modest
399 sea ice growth around the Antarctic continent to the ~35 ppm initial CO₂ drawdown event.
400 While this is theoretical and cannot be adequately addressed in this analysis, it is worthy of
401 deeper consideration.

402 The second possible explanation involves changes in the global overturning circulation.
403 Kohfeld & Chase (2017) previously examined the timing of changes in $\delta^{13}\text{C}$ of benthic
404 foraminifera solely from the Atlantic basin and observed that the largest changes in AMOC
405 coincided with the mid-glacial reductions in atmospheric carbon dioxide changes mentioned
406 above. Subsequent work of O'Neill et al. (2020) examined whole-ocean changes in $\delta^{13}\text{C}$ of

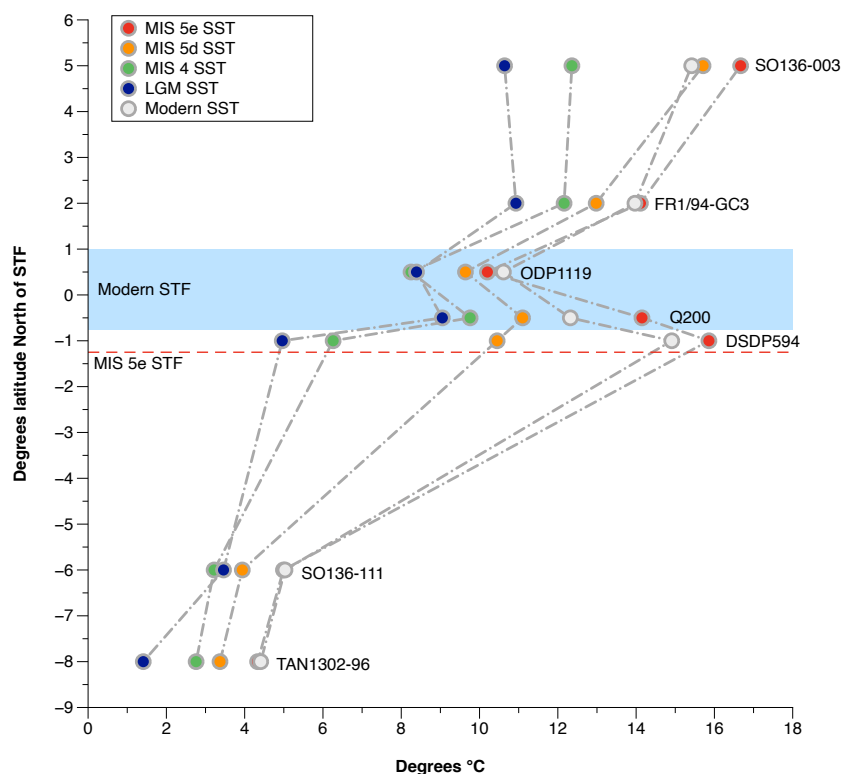


407 benthic foraminifera and noted that the separation between $\delta^{13}\text{C}$ values of abyssal and deep
408 ocean waters were actually initiated between MIS 5d and MIS 5a (114 to 71 ka). Evidence for
409 early changes in abyssal circulation have also been detected in Indian Ocean $\delta^{13}\text{C}$ records
410 (Govin et al., 2009), and more recently in Indian Ocean ϵNd records (Williams et al., 2021),
411 suggesting that the abyssal ocean may have responded to sea ice changes around the Antarctic
412 continent early in the glacial cycle. If indications of an early-glacial response in the global ocean
413 circulation in the Indo-Pacific are correct, these data may also point to an elevated importance
414 of sea ice near the Antarctic continent in triggering early, deep-ocean overturning changes.

415 The third possible explanation involves changes in surface ocean temperature gradients
416 in the Southern Ocean, and how they could influence air-sea gas exchange. Several recent
417 studies have pointed to the importance of changes to air-sea disequilibrium as a key
418 contributor to CO_2 uptake in the Southern Ocean (Eggleston & Galbraith, 2018; Marzocchi &
419 Jansen 2019; Khatiwala et al. 2019). Khatiwala et al. (2019) suggested that modelling studies
420 have traditionally underrepresented (or neglected) the role of air-sea disequilibrium in
421 amplifying the impact of cooling on potential CO_2 sequestration in the mid-high southern
422 latitudes during glacial periods. They argue that when the full effects of air-sea disequilibrium
423 are considered, ocean cooling can result in a 44 ppm decrease due to temperature-based
424 solubility effects alone. They attributed this increased impact of SSTs to a reduction in sea-
425 surface temperature gradients explicitly in polar mid-latitude regions (roughly between 40° and
426 60° north and south). If we compare the SST gradients in the southwest Pacific sector over the
427 last glacial-interglacial cycle (Figure 6), we see an early cooling response between MIS 5e-d
428 corresponding to roughly half of the full glacial cooling, specifically in the cores located south of
429 the modern STF (for core list, see Table B1 in Appendix B). While not quantified, Bianchi &
430 Gersonde (2002) also describe a weakening of meridional SST gradients between the
431 Subantarctic and Antarctic Zones during MIS 5d in the Atlantic sector. Although this analysis is
432 based on sparse data, our SST reconstructions are consistent with the idea that surface ocean
433 cooling, a weakening of meridional SST gradients, and changes to the overall air-sea
434 disequilibrium could be responsible for at least some portion of the early CO_2 drawdown.



435 Further SST estimates from the region, and from the global ocean, are needed to substantiate
436 this hypothesis.



437 **Figure 6:** SST estimates from 7 cores located in the southwestern Pacific. SSTs used were 5-
438 point averages (depending on sampling resolution) taken at MIS peaks/median dates in
439 accordance with boundaries outlined in Lisiecki & Raymo, (2005). Due to the complex
440 circulation and frontal structures in the region, cores were plotted in +/- distance from the
441 average position of the modern STF. Cores used include: SO136-GC3 (SSTs calculated from
442 alkenones, Pelejero et al., 2006); FR1/94-GC3 (alkenones, Pelejero et al., 2006); ODP 181-1119
443 (PF-MAT, Hayward et al., 2008); DSDP594 (PF-MAT, Schaefer et al., 2005); Q200 (PF-MAT,
444 Weaver et al., 1998); SO136-111 (D-MAT, Crosta et al., 2004); and TAN1302-96 (D-MAT; *this*
445 *study*).

446

447 4.4 Sea Ice Expansion and Ocean Circulation

448 Although the TAN1302-96 wSIC record suggests that sea ice was largely absent at the
449 core site until the mid-glacial (~65 ka), the observed changes in sea ice throughout the glacial-



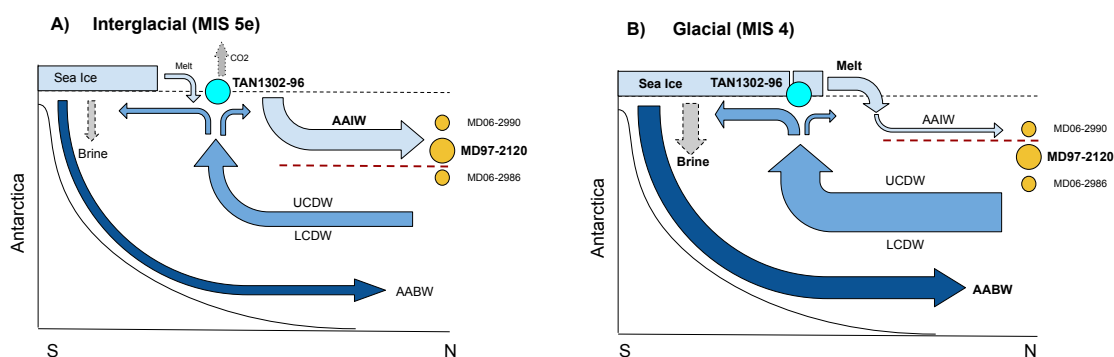
450 interglacial cycle may be linked to regional fluctuations in Antarctic Intermediate Water (AAIW)
451 subduction. The annual growth and decay of Antarctic sea ice plays a critical role in regional
452 water mass formation. Brine rejection results in net buoyancy loss in regions of sea ice
453 formation, while subsequent melt results in freshwater inputs and net buoyancy gains near the
454 ice margin (Shin et al., 2003; Pellichero et al., 2018). This increased freshwater input and
455 buoyancy gain near the ice margin can hinder AAIW subduction, with direct and indirect
456 impacts on both the upper and lower branches of the meridional overturning circulation
457 (Pellichero et al. 2018).

458 Previous research has used $\delta^{13}\text{C}$ in benthic foraminifera to track changes in the depth of
459 the interface between AAIW and Upper Circumpolar Deep Water (UCDW) (Pahnke and Zahn,
460 2005; Ronge et al., 2015). Low $\delta^{13}\text{C}$ values are linked to high nutrient concentrations found at
461 depths below ~ 1500 m in the UCDW, and higher $\delta^{13}\text{C}$ values are associated with the shallower
462 AAIW waters (Figure 5). Marine sediment core MD97-2120 (45.535°S , 174.9403°E , core depth
463 1210 m) was retrieved from a water depth near the interface between the AAIW and UCDW
464 water masses. Over the last glacial-interglacial cycle, fluctuations in the benthic $\delta^{13}\text{C}$ values
465 from MD97-2120 suggest that the core site was intermittently bathed in AAIW and UCDW, and
466 that the vertical extent of AAIW fluctuated throughout the last glacial-interglacial cycle. Ronge
467 et al. (2015) used the $\delta^{13}\text{C}$ values from MD97-2120 and other core sites to quantify the
468 contributions of AAIW to the waters overlying MD97-2120 (%AAIW, Appendix D). These results
469 suggest that during warm periods, MD97- 2120 exhibits more positive $\delta^{13}\text{C}$ values,
470 corresponding to higher %AAIW, while cooler periods exhibit more negative values,
471 corresponding to lower %AAIW (Figure 5). This means that during cooler periods, the AAIW-
472 UCDW interface shoaled, reducing the total volume of AAIW and indirectly causing an
473 expansion of UCDW (Ronge et al., 2015).

474 Our comparison between %AAIW and regional wSIC estimates suggest a strong link
475 between the two (Figure 5). Specifically, we observe that sea ice expansion occurs during time
476 periods when AAIW has shoaled and UCDW has expanded (i.e., %AAIW is low). In contrast,
477 during periods of low wSIC and warmer summer sea surface temperatures (e.g., MIS 5e),
478 %AAIW is high. This correlation supports the idea that increased concentrations of regional sea



479 ice resulted in a substantial summer freshwater flux into the AAIW source region. This regional
480 freshening likely promoted a shallower subduction of AAIW and a corresponding volumetric
481 expansion of UCDW, which can be seen by the isotopic offset of the $\delta^{13}\text{C}$ values between the
482 reference cores, and also by the increased carbonate dissolution in MD97-2120 during glacial
483 periods (Figure 7) (Pahnke et al., 2003; Ronge et al., 2015). These findings directly link sea ice
484 proxy records to observed changes in ocean circulation and water mass geometry.



485 **Figure 7:** Schematic of changes in southwestern Pacific sector sea ice coverage and water mass
486 geometry between interglacial and glacial stages. **A)** Depicts interglacial conditions where sea
487 ice coverage is minimal and freshwater input from summer sea ice melt is low. This lack of
488 freshwater input allows AAIW to subduct to deeper depths and bath core MD97-2120,
489 capturing the higher $\delta^{13}\text{C}$ signature of the overlying AAIW waters. The AAIW-UCDW interface
490 (red dashed line) is located beneath MD97-2120. CO₂ outgassing is occurring as carbon-rich
491 Circumpolar Deep Waters upwell near Antarctica. **B)** Depicts glacial conditions where sea ice
492 expansion has occurred beyond TAN1302-96, increasing brine rejection, and stabilizing the
493 water column. As a result of the increased sea ice growth, subsequent summer melt increases
494 the freshwater flux into the AAIW source region and increases AAIW buoyancy. This buoyancy
495 gain shoals the AAIW-UCDW interface above core MD97-2120, causing the core site to be
496 bathed in low $\delta^{13}\text{C}$ UCDW. The shoaling of AAIW causes an indirect expansion of CDW,
497 increasing the glacial carbon stocks of the deep ocean while sea ice reduces CO₂ outgassing via
498 the capping mechanism.
499

500 In addition to its influence on regional freshwater forcing and AAIW reductions, these
501 sea ice changes may also coincide with larger-scale deep ocean circulation changes. The most
502 dramatic increases in winter sea ice observed in TAN1302-96 and SO136-111, along with
503 changes in %AAIW, are initiated during MIS 4. These shifts also correspond to basin-wide



504 changes in benthic $\delta^{13}\text{C}$ values in the Atlantic Ocean that suggest a shoaling in the Atlantic
505 Meridional Overturning Circulation (AMOC) during MIS 4 (Oliver et al., 2010; Kohfeld & Chase,
506 2017). Changes in deep ocean circulation are also recorded in ϵNd isotope data in the Indian
507 sector of the Southern Ocean (Wilson et al., 2015), suggesting extensive changes in the AMOC
508 during this period. Recent modelling literature (Marzocchi & Jansen, 2019; Stein et al., 2020)
509 suggests that sea ice formation directly impacts marine carbon storage by increasing density
510 stratification and reducing diapycnal mixing, ultimately leading to CO_2 sequestration of an
511 estimated 30-40 ppm into the deep ocean. Taken collectively, the available data show that sea
512 ice expansion, AAIW-UCDW shoaling, changes in the AMOC, and a decrease in atmospheric CO_2
513 all occur concomitantly during MIS 4 (Figure 5). It appears likely, therefore, that sea ice
514 expansion during this time influenced intermediate water density gradients through increased
515 freshening and consequent shoaling of AAIW. This appears to have occurred while
516 simultaneously influencing deep-ocean density, and therefore stratification, through brine
517 rejection and enhanced deep water formation, which ultimately lead to decreased ventilation
518 (Abernathey et al., 2016). These changes in ocean stratification, combined with the sea ice
519 ‘capping’ mechanism, appear to agree with both the recent modelling efforts (Stein et al., 2020)
520 and observed proxy data, and fit well within the hypothesis that mid-glacial CO_2 variability was
521 primarily the result of a more sluggish overturning circulation (Kohfeld & Chase, 2017).

522

523 **5.0 Summary & Conclusion**

524 This study presents new wSIC and sSST estimates from marine core TAN1302-96,
525 located in the southwestern Pacific sector of the Southern Ocean. We find that the wSIC
526 remained low during the early glacial cycle (130 to 70 ka), expanded during the middle glacial
527 cycle (~65 ka), and reached its maximum just prior to the LGM (~24.5 ka). These results largely
528 agree with nearby core SO136-111 but display some differences in wSIC magnitude with E27-
529 23. This discrepancy may be explained by differences in statistical applications and/or lateral
530 sediment redistribution, although more analysis is required to determine the exact cause(s).

531 The lack of changes in sSSTs and the absence of sea ice over the core site during the
532 early glacial suggests that the sea ice capping mechanism and corresponding surface



533 stratification in this region is an unlikely cause for early CO₂ drawdown, and that alternative
534 hypotheses should be considered when evaluating the mechanism(s) responsible for the initial
535 drawdown. More specifically, we consider the impact of changes in SST gradients between ~40°
536 to 60°S and support the idea that changes in air-sea disequilibrium associated with reduced
537 sea-surface temperature gradients could be a potential mechanism that contributed to early
538 glacial reductions in atmospheric CO₂ concentrations (Khatiwala et al., 2019). Another key
539 consideration is the potentially non-linear response between sea ice expansion and CO₂
540 sequestration potential (i.e., that not all sea ice is equal in its capacity to sequester carbon).
541 More analyses are required to adequately address this.

542 We also observe a strong link between regional sea ice concentrations and vertical
543 fluctuations in the AAIW-UCDW interface. Regional sea ice expansion appears to coincide with
544 the shoaling of AAIW, likely due to the freshwater flux from summer sea ice melt increasing
545 buoyancy in the AAIW formation region. Furthermore, major sea ice expansion and AAIW
546 shoaling occurs during the middle of the glacial cycle and is coincident with previously
547 recognized shoaling in AMOC and mid-glacial atmospheric CO₂ reductions, suggesting a
548 mechanistic link between sea ice and ocean circulation.

549 This paper has focused exclusively on sea ice as a driver of physical changes, but we
550 recognize that these changes in sea ice will be accompanied by multiple processes that interact
551 and compete with each other. Marzocchi & Jansen (2019) note that teasing apart the individual
552 components of CO₂ fluctuations is complicated because of interactions between sea ice
553 capping, air-sea disequilibrium, AABW formation rates, and the biological pump. We recognize
554 that these processes may not act independently, and as such, hope to contribute new data to
555 help advance our collective understanding of the role of sea ice on influencing atmospheric CO₂
556 variability on a glacial-interglacial time scale.

557

558 **6.0 Appendices**

559 **Appendix A: Age Model & Sampling Depths**

560 **Table A1:** Radiocarbon dates taken from TAN130-296. NDFB = Not Distinguishable from Background

561



Lab Code	Sample Material	Core Name	Depth (cm)	$\delta^{13}\text{C}$ (per mil)	$\delta^{13}\text{C}$ (+/-)	% Modern Carbon	1 σ error	Fraction Modern	(+/-)	Radiocarbon Year	1 σ error	Reference
NZA 57105	<i>N. pachyderma</i> and <i>G. bulloides</i>	TAN1302-96	21	1	0.2	/	/	0.5982	0.0018	4127	24	Prebble et al., 2017
NZA 57109	<i>N. pachyderma</i> and <i>G. bulloides</i>	TAN1302-96	50	0.7	0.2	/	/	0.3723	0.0015	7936	32	Prebble et al., 2017
OZX 517	<i>N. pachyderma</i> and <i>G. bulloides</i>	TAN1302-96	63	1	0.1	30.62	0.15	/	/	9505	40	This study
NZA 61429	<i>N. pachyderma</i> and <i>G. bulloides</i>	TAN1302-96	75	0.7	0.2	/	/	0.2373	0.0011	11554	37	Prebble et al., 2017
OZX 518	<i>N. pachyderma</i> and <i>G. bulloides</i>	TAN1302-96	87	-0.1	0.1	19.62	0.11	/	/	13085	45	This study
OZX 519	<i>N. pachyderma</i> and <i>G. bulloides</i>	TAN1302-96	130	1.7	0.1	0.02	0.04	/	/	NDFB	/	This study
OZX 520	<i>N. pachyderma</i> and <i>G. bulloides</i>	TAN1302-96	170	-1.1	0.3	0.03	0.04	/	/	NDFB	/	This study

562
563
564

Table A2: Tie points used in construction of the TAN1302-96 age model

TAN1302-96 Depth (cm)	TAN1302-96 $\delta^{18}\text{O}$	LR04 Age	LR04 $\delta^{18}\text{O}$
110	4.710	18000	5.02
170	3.930	56000	4.35
200	3.782	70000	4.32
260	3.150	115000	3.71
300	3.660	129000	3.9
320	4.350	140000	4.98

565
566
567
568
569

Table A3: Sample depth and corresponding age. Diatom slides using Method 1 used sediment samples that are even (e.g., 10, 20, 30, etc.), while diatom slides using Method 2 used sediment samples that are odd (e.g., 53, 87, etc.). * Indicates the sample was calculated based on linear sedimentation rates.

Sample Depth (cm)	Age	Sample Depth (cm)	Age	Sample Depth (cm)	Age	Sample Depth (cm)	Age
10	1802*	100	16167	197	68849	260	114169
20	3282*	103	16720	200	70541	263	115690
30	4762	107	17784	203	72417	267	117398
40	6252	110	18818	207	75211	270	118536
50	7736	113	20200	210	77358	273	119565
53	8168	117	22364	213	79629	277	120909
57	8727	120	24202	217	82635	280	121881
60	9147	123	26113	220	84965	283	122875
63	9566	127	28672	223	87235	287	124228
67	10469	130	30565	227	90337	290	125296
70	11175	140	37018	230	92635	293	126338
73	11910	150	43401	233	94922	297	127857
77	12716	160	49744	237	97910	300	129151



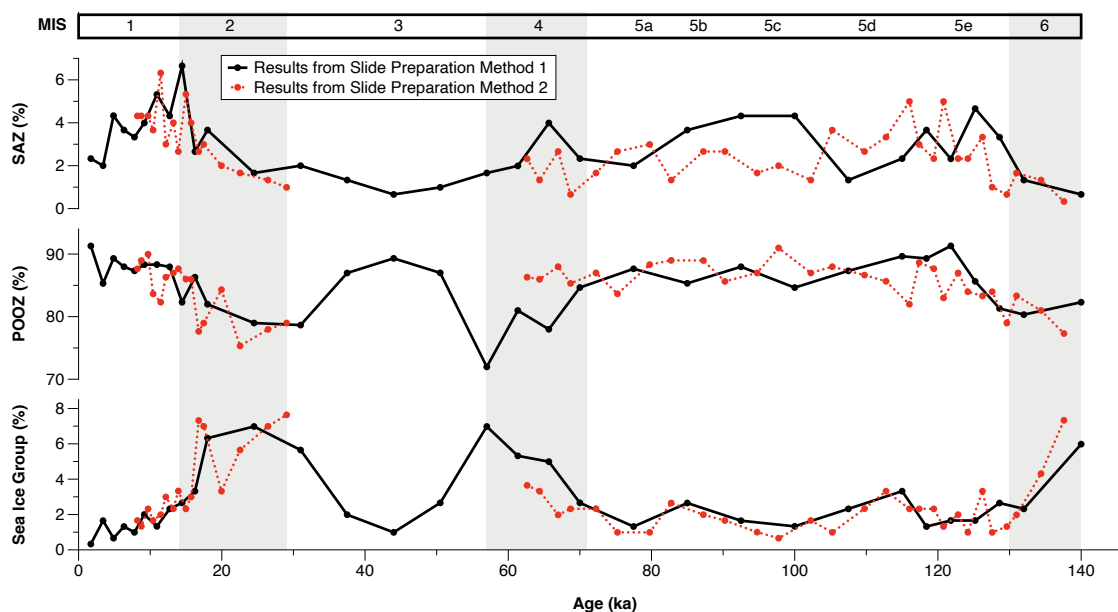
80	13103	170	55709	240	100180	303	130544
83	13504	180	60640	243	102430	307	132573
87	14065	183	62021	247	105398	310	134377
90	14584	187	63905	250	107642	313	136156
93	15066	190	65302	253	109797	317	138193
97	15698	193	66737	257	112475	320	139591

570
571

572 Appendix B: Supporting Information

573 **Table B1:** Information for all cores used in calculating southwestern Pacific sector SST gradients (Figure 7).
574

Core Name	Latitude	Longitude	Depth	Age Model Reference	Data Used	Data Source
TAN1302-96	59.09°S	157.05°E	3099 m	<i>This study</i>	n/a	<i>This study</i>
SO136-111	56.66°S	160.23°E	3912 m	Crosta et al., 2004	wSIC; SST	Crosta et al., 2004; <i>This study</i>
SO136-GC3	42.3°S	169.88°E	958 m	Pelejero et al., 2006; Barrows et al., 2007	δ13C; SST	Pelejero et al., 2006; Ronge et al., 2015
FR1/94-GC3	44.25°S	149.98°E	2667 m	Pelejero et al., 2006	SST	Pelejero et al., 2006
ODP 1119-181	44.75°S	172.39°E	396 m	Wilson et al., 2005	SST	Wilson et al., 2005; Hayward et al., 2008
DSDP 594	45.54°S	174.94°E	1204 m	Nelson et al., 1985; Kowalski & Meyers 1997	SST	Schaefer et al., 2005
Q200	45.99°S	172.02°E	1370 m	Waver et al., 1998	SST	Weaver et al., 1998





575
576 **Figure B1:** Results from diatom slide preparation methods 1 & 2. No notable differences or biases were observed
577 between the two different methods.
578

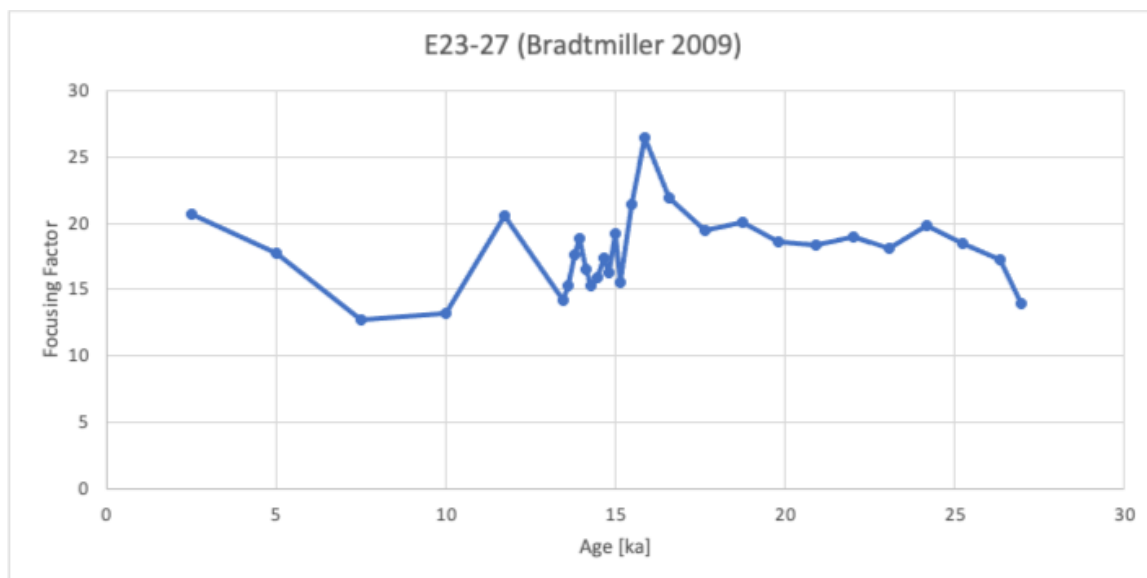
579 **Appendix C: TAN1302-96 and E27-23 Comparison**

581 **Potential Causes for wSIC Estimate Differences**

582 The first potential cause for the observed differences between TAN1302-96 and E27-23
583 wSIC estimates is through the cumulative effects of different laboratory protocols. While it is
584 difficult to determine precisely how much different laboratory protocols could influence the
585 results, we cannot exclude this explanation as a possible contributor to differences in wSIC.

586 The second potential cause for differences in wSIC estimates between E27-23 and
587 TAN1302-96 are differences in counting and identification methods. We believe this is an
588 unlikely cause for the differences observed between E27-23 and TAN1302-96 primarily because
589 of the magnitude of counting discrepancies required to cause a difference of 50% wSIC
590 estimates between the two cores. The close coupling of wSIC estimates between TAN1302-96
591 and SO136-111 over the entire glacial-interglacial cycle supports that a fundamental issue
592 relating to taxonomic identification and/or methodology is an unlikely explanation for the
593 observed wSIC differences.

594 Finally, the fourth potential cause of differing wSIC estimates is selective diatom
595 preservation (e.g., Pichon et al., 1999; Ragueneau et al., 2000). The similarities between
596 TAN1302-96 and SO136-111 wSIC estimates, along with independent indicators in cores E27-23
597 and TAN1302-96, suggest that this is unlikely. For E27-23, Bradtmiller et al. (2009) used the
598 consistent relationship between $^{231}\text{Pa}/^{230}\text{Th}$ ratios and opal fluxes to suggest that dissolution
599 remained relatively constant between the LGM and Holocene periods. In TAN1302-96, we
600 assigned a semi-quantitative diatom preservation value between 1 (extreme dissolution) and 4
601 (virtually perfect preservation) for each counted specimen. The average preservation of
602 diatoms for the entire core was 3.38 ± 0.13 , with no observed bias based on sedimentation rate
603 or MIS. This assessment, although semi-qualitative, suggests that preservation remained
604 relatively constant (and good) throughout TAN1302-96, and is therefore unlikely to cause large
605 differences in wSIC between the two cores.



606
607 **Figure C1:** Preliminary focusing factor (FF) values for E27-23. These results suggest notable lateral sediment
608 redistribution over the last 26 ka, requiring further analysis (Bradt Miller et al., 2009).
609

610 **Appendix D: %AAIW Calculation**

611 The calculation of %AAIW in this study is the same as was used in Ronge et al. (2015):

$$612 \quad \%AAIW = (\delta^{13}C_{MD97-2120} - \delta^{13}C_{MD06-2986}) / (\delta^{13}C_{MD06-2990} - \delta^{13}C_{MD06-2986}) * 100$$

614
615 All core information for MD97-2120, MD06-2986, and MD06-2990, along with supporting
616 supplemental information can be found through the original publication.
617

618 **7.0 Data Availability**

619 All data has been submitted to Pangaea (PDI-29255) and is awaiting publication. Once Pangaea
620 has published the dataset, the corresponding author will supply the DOI.

621

622 **8.0 Author Contributions**

623 The authors confirm that the contributions to this paper are as follows: study conception and
624 design: KK, HB; author data collection: JJ, KK, HB, XC, ML, GD, ZC, AL; analysis and interpretation
625 of results: JJ, KK, HB, XC, ZC, AL, HA, GJ; draft manuscript preparation and/or editing: JJ, KK, HB,



626 XC, GD, ZC, AL, HA, GJ. All authors reviewed the results and approved the final version of the
627 manuscript.

628

629 **9.0 Competing Interests**

630 The authors declare that they have no conflict of interest.

631

632 **10.0 Acknowledgements**

633 This work was supported by a Canadian Natural Sciences and Engineering Research
634 Council grant (Discovery Grant RGPIN342251) to Karen Kohfeld. Travel funding for workshop
635 collaboration was provided to Jacob Jones by a Past Global Changes (PAGES) grant to the Cycles
636 of Sea Ice Dynamics in the Earth System (C-SIDE) Working Group. Rachel Meyne (Colgate
637 University) assisted with slide preparation; Maureen Soon (University of British Columbia)
638 assisted with opal concentration measurements; Marlow Pellatt (Parks Canada) assisted with
639 project conceptualization and guidance. The TAN1302-96 core was collected during the
640 TAN1302 RV Tangaroa voyage to the Mertz Polynya. We would like to thank the Voyage leader
641 Dr. Mike Williams and Captain Evan Solly and the crew, technicians and scientists involved in
642 the TAN1302 voyage. The voyage was co-funded by NIWA, Australian, and French research
643 funding. We acknowledge Dr. Andrew Kingston for running the stable isotopes at NIWA. We
644 acknowledge ANSTO grant AP11676 for funding the additional radiocarbon dates. This research
645 was partially supported by the Australian Government through the Australian Research
646 Council's Discovery Projects funding scheme (project DP180102357, awarded to Zanna Chase
647 and Helen Bostock).

648

649 **11.0 References**

650

651 Abernathey, R. P., Cerovecki, I., Holland, P. R., Newsom, E., Mazloff, M., and Talley, L. D. (2016).
652 Water-mass transformation by sea ice in the upper branch of the Southern Ocean overturning.
653 *Nature Geoscience*, 9(8), 596–601. <https://doi.org/10.1038/ngeo2749>

654



- 655 Archer, D.E., Martin, P.A., Milovich, J., Brovkin, V., Plattner, G.K., and Ashendel, C. (2003).
656 Model sensitivity in the effect of Antarctic sea ice and stratification on atmospheric
657 pCO₂. *Paleoceanography*, 18(1): 1012. <https://doi.org/10.1029/2002PA000760>
658
- 659 Benz, V., Esper, O., Gersonde, R., Lamy, F., and Tiedemann, R. (2016). Last Glacial Maximum sea
660 surface temperature and sea-ice extent in the Pacific sector of the Southern Ocean. *Quaternary*
661 *Science Reviews*, 146: 216–237. <https://doi.org/10.1016/j.quascirev.2016.06.006>
662
- 663 Bianchi, C., and Gersonde, R. (2002). The Southern Ocean surface between Marine Isotope
664 Stages 6 and 5d: shape and timing of climate changes. *Paleogeography, Paleoclimatology,*
665 *Paleoecology*, 187: 151–177.
666
- 667 Bereiter, B., Eggleston, S., Schmitt, J., Nehrbass-Ahles, C., Stocker, T.F., Fischer, H., Kipfstuhl, S.,
668 and Chappellaz, J. (2015). Revision of the EPICA Dome C CO₂ record from 800 to 600 kyr before
669 present. *Geophysical Research Letters*, 42(2): 542–549. <https://doi.org/10.1002/2014GL061957>
670
- 671 Bostock, H., Hayward, B., Neil, H., Sabaa, A., & Scott, G. (2015). Changes in the position of the
672 Subtropical Front south of New Zealand since the last glacial period. *Paleoceanography*, 30(7),
673 824–844. <https://doi.org/10.1002/2014PA002652>
674
- 675 Bouttes, N., Paillard, D., and Roche, D. M. (2010). Impact of brine-induced stratification on the
676 glacial carbon cycle. *Climate of the Past*, 6(5): 575–589. <https://doi.org/10.5194/cp-6-575-2010>
677
- 678 Bradtmiller, L.I., Anderson, R.F., Fleisher, M.Q. and Burckle, L.H. (2009). Comparing glacial and
679 Holocene opal fluxes in the Pacific sector of the Southern Ocean. *Paleoceanography*, 24(2),
680 PA2214–n/a. <https://doi.org/10.1029/2008PA001693>
681
- 682 Butzin, M., Köhler, P., and Lohmann, G. (2017). Marine radiocarbon reservoir age simulations
683 for the past 50,000 years. *Geophysical Research Letters*, 44(16), 8473–8480.
684 <https://doi.org/10.1002/2017GL074688>
685
- 686 Butzin, M., Heaton, T.J., Köhler, P., and Lohmann, G. (2020). A short note on marine reservoir
687 age simulations used in INTCAL20. *Radiocarbon*, 62(4), 1–7.
688 <https://doi.org/10.1017/RDC.2020.9>
689
- 690 Cefarelli, A.O., Ferrario, M.E., Almandoz, G.O., Atencio, A.G., Akselman, R., and Vernet, M.
691 (2010). Diversity of the diatom genus *Fragilariopsis* in the Argentine Sea and Antarctic waters:
692 morphology, distribution and abundance. *Polar Biology*, 33(11): 1463–1484.
693 <https://doi.org/10.1007/s00300-010-0794-z>
694
- 695 Crosta, X., Pichon, J.-J., and Burckle, L.H., (1998). Application of modern analog technique to
696 marine Antarctic diatoms: reconstruction of maximum sea-ice extent at the Last Glacial
697 Maximum. *Paleoceanography*, 13: 284–297.
698



- 699 Crosta, X., Sturm, A., Armand, L., and Pichon, J.-J., (2004). Late Quaternary sea ice history in the
700 Indian sector of the Southern Ocean as recorded by diatom assemblages. *Marine*
701 *Micropaleontology*, 50: 209–223.
702
- 703 Crosta, X., Shukla, S.K., Ther, O., Ikehara, M., Yamane, M., and Yokoyama, Y. (2020). Last
704 Abundant Appearance Datum of *Hemidiscus karstenii* driven by climate change. *Marine*
705 *Micropaleontology*, 157: 101861. <https://doi.org/10.1016/j.marmicro.2020.101861>
706
- 707 Delille, B., Vancoppenolle, M., Geilfus, N.X., Tilbrook, B., Lannuzel, D., Schoemann, V.,
708 Becquevort, S., Carnat, G., Delille, D., Lancelot, C., Chou, L., Dieckmann, G.S., and Tison, J.L.
709 (2014). Southern Ocean CO₂ sink: The contribution of sea ice. *Journal of Geophysical Research*,
710 119(9): 6340-3655. <https://doi.org/10.1002/2014JC009941>
711
- 712 Eggleston, S., and E.D. Galbraith. (2018). The devil's in the disequilibrium: multi-component
713 analysis of dissolved carbon and oxygen changes under a broad range of forcings in a general
714 circulation model. *Biogeosciences* 15: 3761-3777.
715
- 716 Esper, O., and Gersonde, R. (2014). New tools for the reconstruction of Pleistocene Antarctic
717 Sea ice. *Palaeogeography, Paleoclimatology, Paleoecology*, 399: 260–283.
718 <https://doi.org/10.1016/j.palaeo.2014.01.019>
719
- 720 Fenner, J., Schrader, H., and Wienigk, H. (1976). Diatom Phytoplankton Studies in the Southern
721 Pacific Ocean, Composition and Correlation to the Antarctic Convergence and Its
722 Paleocological Significance.
723
- 724 Ferrari, R., Jansen, M.F., Adkins, J.F., Burke, A., Stewart, A.L., Thompson, A.F. (2014). Antarctic
725 sea ice control on ocean circulation in present and glacial times. *Proceedings of the National*
726 *Academy of Sciences of the United States of America*, 111: 8753–8758.
727
- 728 Ferry, A.J., Crosta, X., Quilty, P.G., Fink, D., Howard, W., and Armand, L.K. (2015). First records
729 of winter sea ice concentration in the southwest Pacific sector of the Southern
730 Ocean. *Paleoceanography*, 30(11): 1525–1539. <https://doi.org/10.1002/2014pa002764>
731
- 732 Froelich, P. N. (1991). Biogenic opal and carbonate accumulation rates in the Subantarctic South
733 Atlantic: The late Neogene of Meteor Rise site 704. *Proceedings of the Ocean Drilling Program,*
734 *Scientific Results*, 120, 515–549.
735
- 736 Fryxell, G.A., Hasle, G.R. (1976). The genus *Thalassiosira*: some species with a modified ring of
737 central strutted processes. *Nova Hedwigia Beihefte*, 54: 67-98.
738
- 739 Fryxell, G.A., Hasle, G.R., (1980). The marine diatom *Thalassiosira oestrupii*: structure,
740 taxonomy and distribution. *American Journal of Botany*, 67: 804-814.
741



- 742 Galbraith, E., and de Lavergne, C. (2019). Response of a comprehensive climate model to a
743 broad range of external forcings: relevance for deep ocean ventilation and the development of
744 late Cenozoic ice ages. *Climate Dynamics*, 52(1), 653–679. [https://doi.org/10.1007/s00382-018-](https://doi.org/10.1007/s00382-018-4157-8)
745 [4157-8](https://doi.org/10.1007/s00382-018-4157-8)
746
- 747 Gersonde, R., and Zielinski, U. (2000). The reconstruction of late Quaternary Antarctic sea-ice
748 distribution—the use of diatoms as a proxy for sea-ice. *Palaeogeography, Palaeoclimatology,*
749 *Palaeoecology*, 162(3), 263–286. [https://doi.org/10.1016/S0031-0182\(00\)00131-0](https://doi.org/10.1016/S0031-0182(00)00131-0)
750
- 751 Gersonde, R., Crosta, X., Abelmann, A., and Armand, L. (2005). Sea-surface temperature and sea
752 ice distribution of the Southern Ocean at the EPILOG last Glacial Maximum—a circum-Antarctic
753 view based on siliceous microfossil records. *Quaternary Science Reviews*, 24 (7–9): 869–896.
754
- 755 Ghadi, P., Nair, A., Crosta, X., Mohan, R., Manoj, M.C, and Meloth, T. (2020). Antarctic sea-ice
756 and palaeoproductivity variation over the last 156,000 years in the Indian sector of Southern
757 Ocean. *Marine Micropaleontology*, 160: 101894.
758 <https://doi.org/10.1016/j.marmicro.2020.101894>
759
- 760 Govin, A., Michel, E., Labeyrie, L., Waelbroeck, C., Dewilde, F., and Jansen, E. (2009), Evidence
761 for northward expansion of Antarctic Bottom Water mass in the Southern Ocean during the last
762 glacial inception, *Paleoceanography*, 24, PA1202, doi:[10.1029/2008PA001603](https://doi.org/10.1029/2008PA001603).
763
- 764 Guiot, J., de Beaulieu, J.L., Cheddadi, R., David, F., Ponel, P., Reille, M. (1993). The climate of
765 western Europe during the last Glacial/Interglacial cycle derived from pollen and insect
766 remains. *Palaeogeography, Palaeoclimatology, Palaeoecology*, 103: 73–93.
767
- 768 Guiot, J., and de Vernal, A. (2011). Is spatial autocorrelation introducing biases in the apparent
769 accuracy of paleoclimatic reconstructions? *Quaternary Science Reviews*, 30(15-16): 1965–1972.
770 <https://doi.org/10.1016/j.quascirev.2011.04.022>
771
- 772 Hasle G.R., and Syvertsen, E.E. (1997) Marine diatoms. In: Tomas CR (ed) Identifying marine
773 phytoplankton. Academic Press, pp 5–385.
774
- 775 Heaton, T., Köhler, P., Butzin, M., Bard, E., Reimer, R., Austin, W., Bronk Ramsey, C., Grootes, P.,
776 Hughen, K., Kromer, B., Reimer, P., Adkins, J., Burke, A., Cook, M., Olsen, J., and Skinner, L.
777 (2020). Marine20—The Marine Radiocarbon Age Calibration Curve (0–55,000 cal
778 BP). *Radiocarbon*, 62(4), 779–820. <https://doi.org/10.1017/RDC.2020.68>
779
- 780 Johansen, J.R., and Fryxell, G.A. (1985). The genus *Thalassiosira* (Bacillariophyceae): studies on
781 species occurring south of the Antarctic Convergence Zone. *Deep-Sea Research. Part B.*
782 *Oceanographic Literature Review*, 32(12): 1050. [https://doi.org/10.1016/0198-0254\(85\)94033-6](https://doi.org/10.1016/0198-0254(85)94033-6)
783



- 784 Khatiwala, S, Schmittner, A, and Muglia, J. (2019). Air-sea disequilibrium enhances ocean
785 carbon storage during glacial periods. *Science Advances*, 5(6), eaaw4981–eaaw4981.
786 <https://doi.org/10.1126/sciadv.aaw4981>
787
- 788 Kohfeld, K.E., and Chase, Z. (2017). Temporal evolution of mechanisms controlling ocean carbon
789 uptake during the last glacial cycle. *Earth and Planetary Science Letters*, 472: 206–215.
790 <https://doi.org/10.1016/j.epsl.2017.05.015>
791
- 792 Kohfeld, K.E., and Ridgwell, A. (2009). Glacial-Interglacial Variability in Atmospheric CO₂ – Surface
793 Ocean-Lower Atmospheric Processes (eds C. L. Quéré and E. S. Saltzman), American
794 Geophysical Union, Washington D.C.
795
- 796 Lisiecki, L.E., and Raymo, M.E., (2005). A Pliocene–Pleistocene stack of 57 globally dis- tributed
797 benthic $\delta^{18}\text{O}$ records. *Paleoceanography*, 20(1): 1-17. <https://doi.org/10.1029/2004PA001071>
798
- 799 Locarnini, R.A., Mishonov, A.V., Antonov, J.I., Boyer, T.P., Garcia, H.E., Baranova, O.K., Zweng,
800 M.M., Paver, C.R., Reagan, J.R., Johnson, D.R., Hamilton, M., Seidov, D. (2013). World Ocean
801 atlas 2013, volume 1: Temperature. In: Levitus, S. (Ed.), A. Mishonov Technical. Vol. 73. pp. 40.
802 (NOAA Atlas NESDIS).
803
- 804 Lougheed, B. C., and Obrochta, S. P. (2019). A Rapid, Deterministic Age-Depth Modeling Routine
805 for Geological Sequences With Inherent Depth Uncertainty. *Paleoceanography and*
806 *Paleoclimatology*, 34(1), 122–133. <https://doi.org/10.1029/2018PA003457>
807
- 808 Marzocchi, A., & Jansen, M.F. (2019). Global cooling linked to increased glacial carbon storage
809 via changes in Antarctic sea ice. *Nature Geoscience*, 12(12): 1001–1005.
810 <https://doi.org/10.1038/s41561-019-0466-8>
811
- 812 Mix, A.C., Bard, E., & Schneider, R. (2001). Environmental processes of the ice age: land, oceans,
813 glaciers (EPILOG). *Quaternary Science Reviews*, 20(4), 627–657. [https://doi.org/10.1016/S0277-3791\(00\)00145-1](https://doi.org/10.1016/S0277-3791(00)00145-1)
814
815
- 816 Morales Maqueda, M.A., and Rahmstorf, S. (2002). Did Antarctic sea-ice expansion cause glacial
817 CO₂ decline? *Geophysical Research Letters*, 29(1), 1011–11–3.
818 <https://doi.org/10.1029/2001GL013240>
819
- 820 Oliver, K. I. C., Hoogakker, B. A. A., Crowhurst, S., Henderson, G. M., Rickaby, R. E. M., Edwards,
821 N. R., and Elderfield, H. (2009). A synthesis of marine sediment core $\delta^{13}\text{C}$ data over the last
822 150 000 years. *Climate of the Past Discussions*, 5(6): 2497–2554. <https://doi.org/10.5194/cpd-5-2497-2009>
823
824
- 825 O'Neill, C.M., Hogg, A.M., Ellwood, M.J., Opdyke, B.N., & Eggins, S.M. (2021). Sequential
826 changes in ocean circulation and biological export productivity during the last glacial–



- 827 interglacial cycle: a model–data study. *Climate of the Past*, 17(1), 171–201.
828 <https://doi.org/10.5194/cp-17-171-2021>
829
- 830 Pahnke, K., Zahn, R., Elderfield, H., and Schulz, M. (2003), 340,000-year centennial-scale marine
831 record of Southern Hemisphere climatic oscillation, *Science*, 301: 948–952.
832
- 833 Pahnke, K., and Zahn, R. (2005). Southern Hemisphere Water Mass Conversion Linked with
834 North Atlantic Climate Variability. *Science (American Association for the Advancement of*
835 *Science)*, 307(5716): 1741–1746. <https://doi.org/10.1126/science.1102163>
836
- 837 Paterne, M., Michel, E., and Héros, V. (2019). Variability of marine 14C reservoir ages in the
838 Southern Ocean highlighting circulation changes between 1910 and 1950. *Earth and Planetary*
839 *Science Letters*, 511, 99–104. <https://doi.org/10.1016/j.epsl.2019.01.029f>
840
- 841 Pellichero, V., Sallée, J.B., Chapman, C., and Downes, S. (2018). The Southern Ocean meridional
842 overturning in the sea-ice sector is driven by freshwater fluxes. *Nature Communications*, 9(1),
843 1789–9. <https://doi.org/10.1038/s41467-018-04101-2>
844
- 845 Pichon, J.J., Bareille, G., Labracherie, M., Labeyrie, L.D., Baudrimont, A. & Turon, J.L. (1992).
846 Quantification of the Biogenic Silica Dissolution in Southern Ocean Sediments. *Quaternary*
847 *Research*, 37(3), 361–378. [https://doi.org/10.1016/0033-5894\(92\)90073-R](https://doi.org/10.1016/0033-5894(92)90073-R)
848
- 849 Prebble, J. G., Bostock, H. C., Cortese, G., Lorrey, A. M., Hayward, B. W., Calvo, E., Northcote, L.
850 C., Scott, G. H., and Neil, H. L. (2017). Evidence for a Holocene Climatic Optimum in the
851 southwest Pacific: A multiproxy study. *Paleoceanography*, 32(8), 763–779.
852 <https://doi.org/10.1002/2016PA003065>
853
- 854 Ragueneau, O., Tréguer, P., Leynaert, A., Anderson, R.F., Brzezinski, M.A., DeMaster, D.J.,
855 Dugdale, R.C., Dymond, J., Fischer, G., François, R., Heinze, C., Maier-Reimer, E., Martin-
856 Jézéquel, V., Nelson, D.M., & Quéguiner, B. (2000). A review of the Si cycle in the modern
857 ocean: recent progress and missing gaps in the application of biogenic opal as a
858 paleoproductivity proxy. *Global and Planetary Change*, 26(4), 317–365.
859 [https://doi.org/10.1016/S0921-8181\(00\)00052-7](https://doi.org/10.1016/S0921-8181(00)00052-7)
860
- 861 Renberg, I. (1990). A procedure for preparing large sets of diatom slides from sediment
862 cores. *Journal of Paleolimnology*, 4(1): 87-90. <https://doi.org/10.1007/bf00208301>
863
- 864 Reynolds, R., Rayner, N., Smith, T., Stokes, D., and Wang, W. (2002). An Improved In Situ and
865 Satellite SST Analysis for Climate. *Journal of Climate*, 15(13), 1609–1625.
866 [https://doi.org/10.1175/1520-0442\(2002\)015<1609:AIISAS>2.0.CO;2](https://doi.org/10.1175/1520-0442(2002)015<1609:AIISAS>2.0.CO;2)
867
- 868 Reynolds, R., Smith, T., Chunying, L., Chelton, D., Casey, K., & Schlax, M. (2007). Daily High-
869 Resolution-Blended Analyses for Sea Surface Temperature. *Journal of Climate*, 20(22), 5473–
870 5496. <https://doi.org/10.1175/2007JCLI1824.1>



- 871
872 Ronge, T.A., Steph, S., Tiedemann, R., Prange, M., Merkel, U., Nürnberg, D., and Kuhn, G.
873 (2015). Pushing the boundaries: Glacial/interglacial variability of intermediate and deep waters
874 in the southwest Pacific over the last 350,000 years. *Paleoceanography*, 30(2): 23–38.
875 <https://doi.org/10.1002/2014pa002727>
876
877 Rutgers van der Loeff, M.M., Cassar, N., Nicolaus, M., Rabe, B., and Stimac, I. (2014). The
878 influence of sea ice cover on air-sea gas exchange estimated with radon-222 profiles. *Journal of*
879 *Geophysical Research, Oceans*, 119(5): 2735–2751. <https://doi.org/10.1002/2013jc009321>
880
881 Schlitzer, R. (2005). Interactive analysis and visualization of geoscience data with Ocean Data
882 View. *Computers and Geoscience*, 28: 1211–1218. [https://doi.org/10.1016/S0098-](https://doi.org/10.1016/S0098-3004(02)00040-7)
883 [3004\(02\)00040-7](https://doi.org/10.1016/S0098-3004(02)00040-7)
884
885 Schneider Mor, A., Yam, R., Bianchi, C., Kunz-Pirrung, M., Gersonde, R., & Shemesh, A. (2012).
886 Variable sequence of events during the past seven terminations in two deep-sea cores from the
887 Southern Ocean. *Quaternary Research*, 77(2), 317–325.
888 <https://doi.org/10.1016/j.yqres.2011.11.006>
889
890 Shin, S.I., Liu, Z., Otto-Bliesner, B., Kutzbach, J., & Vavrus, Stephen J. (2003). Southern Ocean
891 sea-ice control of the glacial North Atlantic thermohaline circulation. *Geophysical Research*
892 *Letters*, 30(2), 1096–n/a. <https://doi.org/10.1029/2002GL015513>
893
894 Sigman, D., and Boyle, E. (2000) Glacial/Interglacial variations in atmospheric carbon dioxide.
895 *Nature (London)*, 407(6806): 859-869. <https://doi.org/10.1038/35038000>
896
897 Smith, R. O., Vennell, R., Bostock, H. C., & Williams, M. J. (2013). Interaction of the subtropical
898 front with topography around southern New Zealand. *Deep-Sea Research. Part I,*
899 *Oceanographic Research Papers*, 76, 13–26. <https://doi.org/10.1016/j.dsr.2013.02.007>
900
901 Sokolov, S., & Rintoul, S. (2009). Circumpolar structure and distribution of the Antarctic
902 Circumpolar Current fronts: 2. Variability and relationship to sea surface height. *Journal of*
903 *Geophysical Research: Oceans*, 114(C11), n/a–n/a. <https://doi.org/10.1029/2008JC005248>
904
905 Stein, K., Timmermann, A., Kwon, E.Y., and Friedrich, T. (2020). Timing and magnitude of
906 Southern Ocean sea ice/carbon cycle feedbacks. *Proceedings of the National Academy of*
907 *Sciences*, 117(9): 4498–4504. <https://doi.org/10.1073/pnas.1908670117>
908
909 Stephens, B.B., and Keeling, R.F. (2000). The influence of Antarctic sea ice on glacial–interglacial
910 CO₂ variations. *Nature (London)*, 404(6774): 171–174. <https://doi.org/10.1038/35004556>
911
912 Studer, A. S., Sigman, D.M., Martínez-García, A., Benz, V., Winckler, G., Kuhn, G., Esper, O.,
913 Lamy, F., Jaccard, S.L., Wacker, L., Oleynik, S., Gersonde, R., and Haug, G.H. (2015). Antarctic



- 914 Zone nutrient conditions during the last two glacial cycles. *Paleoceanography*, 30(7): 845–862.
915 <https://doi.org/10.1002/2014PA002745>
916
- 917 Sun, X., and Matsumoto, K. (2010). Effects of sea ice on atmospheric pCO₂: A revised view and
918 implications for glacial and future climates. *Journal of Geophysical Research:*
919 *Biogeosciences*, 115(G2), n/a–n/a. <https://doi.org/10.1029/2009JG001023>
920
- 921 Toggweiler, J. R. (1999). Variation of atmospheric CO₂ by ventilation of the ocean's deepest
922 water. *Paleoceanography*, 14(5): 571–588. <https://doi.org/10.1029/1999PA900033>
923
- 924 Warnock, J.P., and Scherer, R.P. (2015). A revised method for determining the absolute
925 abundance of diatoms. *Journal of Paleolimnology*, 53(1): 157–163.
926 <https://doi.org/10.1007/s10933-014-9808-0>
927
- 928 Wilks, J. V., and Armand, L. K. (2017). Diversity and taxonomic identification of *Shionodiscus*
929 spp. in the Australian sector of the Subantarctic Zone. *Diatom Research*, 32(3): 295–307.
930 <https://doi.org/10.1080/0269249X.2017.1365015>
931
- 932 Williams, M. J. (2013). Voyage Report TAN1302, Mertz Polynya (Tech. Rep.). Wellington:
933 National Institute of Water and Atmospheric Research (NIWA).
934
- 935 Williams, T.J., Martin, E.E., Sikes, E., Starr, A., Umling, N.E., & Glaubke, R. (2021). Neodymium
936 isotope evidence for coupled Southern Ocean circulation and Antarctic climate throughout the
937 last 118,000 years. *Quaternary Science Reviews*, 260, 106915.
938 <https://doi.org/10.1016/j.quascirev.2021.106915>
939
- 940 Wilson, D.J., Piotrowski, A.M., Galy, A., and Banakar, V.K. (2015). Interhemispheric controls on
941 deep ocean circulation and carbon chemistry during the last two glacial cycles.
942 *Paleoceanography*, 30: 621–641.
943
- 944 Wolff, E.W., Barbante, C., Becagli, S., Bigler, M., Boutron, C.F., Castellano, E., de Angelis, M.,
945 Federer, U., Fischer, H., Fundel, F., Hansson, M., Hutterli, M., Jonsell, U., Karlin, T., Kaufmann,
946 P., Lambert, F., Littot, G.C., Mulvaney, R., Röthlisberger, R., and Wegner, A. (2010). Changes in
947 environment over the last 800,000 years from chemical analysis of the EPICA Dome C ice
948 core. *Quaternary Science Reviews*, 29(1), 285–295.
949 <https://doi.org/10.1016/j.quascirev.2009.06.013>
950